Available online at www.sciencedirect.com
ScienceDirect
Trans. Nonferrous Met. Soc. China 34(2024) 2455−2475
Transactions of Nonferrous Metals Society of China
www.tnmsc.cn

Modeling and characterization on electroplastic effect during dynamic deformation of 5182-O aluminum alloy

Hong-chun SHANG, Song-chen WANG, Yan-shan LOU

School of Mechanical Engineering, Xi'an Jiaotong University, Xi'an 710049, China

Received 7 January 2023; accepted 5 September 2023

Abstract: The coupling effects of electrical pulse, temperature, strain rate, and strain on the flow behavior and plasticity of 5182-O aluminum alloy were investigated and characterized. The isothermal tensile test and electrically-assisted isothermal tensile test were performed at the same temperature, and three typical models were further embedded in ABAQUS/Explicit for numerical simulation to illustrate the electroplastic effect. The results show that electric pulse reduces the deformation resistance but enhances the elongation greatly. The calibration accuracy of the proposed modified Lim−Huh model for highly nonlinear and coupled dynamic hardening behavior is not much improved compared to the modified Kocks−Mecking model. Moreover, the artificial neural network model is very suitable to describe the macromechenical response of materials under the coupling effect of different variables.

Key words: machine learning; aluminium alloy; electroplastic effect; coupling effect; finite element analysis

1 Introduction

Aluminum alloy is considered as one of the most competitive lightweight materials in aerospace, transportation and other fields due to its excellent comprehensive mechanical properties, such as low density, high specific strength and high specific stiffness [1]. The poor formability of 5182-O aluminum alloy at room temperature leads to defects such as cracks and springback during plastic deformation. Therefore, hot forming is used to satisfy the increasing requirements of the complicated shape and enhanced performance of complex components. However, problems, such as high energy consumption, long production cycle, complex working conditions, and high temperature resistant mold materials, significantly increase the manufacturing cost of hot forming [2,3]. Therefore, in order to improve the forming efficiency and quality, the advanced electrically assisted processing (EAP) to replace the traditional hot forming method is the best choice to achieve energy-saving and high-efficiency production [4]. EAP has a significant effect on reducing the difficulty of manufacturing complex components, optimizing material microstructure, and improving the comprehensive mechanical properties and surface quality [5,6].

The electroplastic effect is that the electrical pulse makes it easier for dislocations to slip in the material lattice [7,8]. During the plastic deformation of metals, the deformation resistance is sharply reduced and the plasticity is greatly improved [9]. Electrons transfer energy to microstructural defects, such as dislocations under the interaction between electrons and dislocations to promote local diffusion rates and local heating [10]. It has been proved that the drifting electrons can effectively improve the thermal activation process of dislocation motion in metallic materials, thus the dislocation motion is

Corresponding author: Yan-shan LOU, Tel: +86-18691836771, E-mail: ys.lou@xjtu.edu.cn
DOI: 10.1016/S1003-6326(24)66553-2

promoted [11−14]. EAP has achieved many contributions as a high-density energy input method in the aspects of microstructure control of metallic materials, improvement of mechanical properties and formability, and development of new advanced forming technologies [15−18]. Electricity is applied to reducing the springback during deformation, and SALANDRO et al [19] significantly reduced the springback rate by up to 77% in electrically assisted air bending.

In recent years, many constitutive models have been proposed or improved to describe the plastic behavior of aluminum alloys [20,21]. The artificial neural network (ANN) model is an emerging phenomenological model with extensive applications in the crystal plasticity [22], rate-dependent plasticity [23−25], isotropic plasticity [26−28], and path-dependent plasticity [29−31]. LI et al [32] introduced the effective aging time as a state variable to describe the effect of different strain rates on the dynamic hardening behavior, and the determined ANN model could predict the nonlinear plastic and fracture responses of DP780. For the highly nonlinear dynamic hardening behavior of coupling effect, SHANG et al [33] conducted a comprehensive study on the factors that affect the prediction accuracy and numerical calculation efficiency of ANN model. JIA et al [34] studied the deformation behavior of 304 austenitic stainless steel over a wide range of strain rates and temperatures.

The objective of this work is to investigate the effect of electrical pulse on the dynamic mechanical responses of 5182-O aluminum alloy and its analytical modelling approached for numerical simulation. The corresponding stress−strain curves were obtained at the same initial temperature by electrically-assisted isothermal tensile test (EAITT) and isothermal tensile test (ITT). The modified Kocks−Mecking (MKM) model and the proposed modified Lim−Huh (MLH) model were used to calibrate the experimental results, respectively. In addition, a single hidden layer ANN model was used to describe the highly nonlinear experimental results considering the numerical calculation time. Finally, all models were implemented in numerical simulations to predict the reaction forces at different strain rates and temperatures. The accurate simulation based on ANN model is beneficial to the optimization of process and structure in the EAP.

2 Experimental

2.1 Mechanical properties testing

The 5182-O aluminum alloy sheet with a thickness of 1.25 mm is cut by laser along the rolling direction to obtain the dogbone specimen with a parallel length of 60 mm. The length of the virtual extensometer for stroke measurement is 30 mm for the dogbone specimen. Based on the principle of digital image correlation (DIC), a 3D XTOP DIC system is used to measure the relative position changes of random black spots on the specimen surface without contact. The synchronous acquisition signals of force and displacement are adjusted for different stretching speeds so that the camera can clearly capture 100−200 images.

The schematic diagram of dynamic tensile equipment is shown in Fig. 1. In order to achieve the strain rates of 0.001, 0.01 and 0.1 s^{-1}, uniaxial tensile tests are carried out at crosshead speeds of 3.6, 36 and 360 mm/min, respectively. The tensile tests are divided into ITT and EAITT according to the heating method. For the ITT, hot air around the

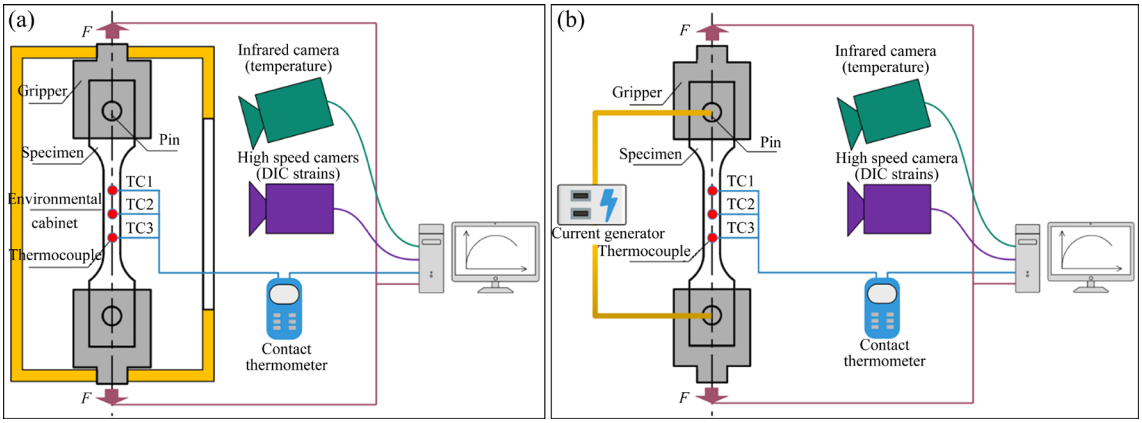

Fig. 1 Schematic diagrams of test: (a) ITT test; (b) EAITT test

resistance wire is blown into the environmental chamber to achieve convection, and then the specimen is stretched after the specified temperature is reached, as shown in Fig. 1(a). The temperature of the specimen during the tensile test is monitored by the UTi260B infrared thermal imaging camera (ITIC). The temperature range is from 258 to 823 K and the thermal sensitivity is less than 0.05 K. Because the accuracy of the temperature measured by the ITIC is greatly affected by the emissivity, there is a deviation when the temperature is measured through the glass of the environmental chamber. The emissivity is calibrated by the temperature of three measuring points in the gauge length of the specimen by K-type thermocouples.

The schematic diagram of the device for tensile test with pulsed electric current is shown in Fig. 1(b). When an electric field is applied to the dogbone specimen in the EAITT, the kinetic energy of the drifting electrons is accelerated and converted into the internal energy of the metal, resulting in an increase in the temperature of the specimen. The temperature measured by the ITIC is also corrected by three K-type thermocouples. In order to achieve the insulating effect, a self-made insulating clamp is inserted with mica sheets in-between to ensure that the current only passes through the sample during the test. Continuous electrical pulses are generated by a commercial pulsed power supply with a rated output current of 1 kA, a voltage of 5 V, a frequency of 50 Hz and a pulse duty cycle of 50%. When a closed loop is formed, the specimen is rapidly heated by the Joule heating effect until the Joule heating and heat loss reach a dynamic equilibrium. The temperature of the specimen reaches a relatively stable value, where the heat loss includes heat conduction with the clamped electrode, convective heat exchange with the surrounding air, and heat radiation from the heating material. The current amplitude is then held constant throughout the tensile test to induce a constant nominal current density based on the initial cross-sectional area [6].

2.2 Microstructure characterization

The microstructures of the specimens near the fracture are characterized by X-ray diffraction (XRD) and transmission electron microscopy (TEM). The XRD analysis of the 5182-O specimens under different conditions is carried out on a D8 Advance diffractometer with Cu K_α radiation at a voltage of 40 kV. Rapid scans are performed from 35° to 105° with a 0.02 (°)/s step and 0.02 s/step acquisition time to analyze the critical phase composition. The TEM samples are mechanically ground and polished to about 70 μm with 400#–2000# grit SiC papers and subsequently punched into 3 mm discs. Finally, TEM foils are prepared by twin-jet electropolishing in a mixed solution of 30 vol.% nitric acid and 70 vol.% methanol at −30 °C. The microstructures of the prepared samples are further characterized by a JEOL JEM-F200 with an accelerating voltage of 200 kV. The fractographs of tensile specimens are examined by scanning electron microscope (SEM), and the fracture mechanisms of 5182-O aluminum alloy under different loading conditions are studied. The test specimens are polished by standard metallographic methods and electrolytically polished for electron backscatter diffraction (EBSD) observation with the accelerating voltage of 20 V and the scanning step size of 0.2 μm. EBSD microstructures and pole figures are obtained by orientation imaging microscopy (OIM) analysis software.

3 Experimental results

3.1 Mechanical properties

Figure 2 shows the temperature and strain distributions of the dogbone specimen at 423 K with a strain rate of 0.1 s^{-1}. The specimen is stretched when it is heated to 423 K by EAITT, and the equivalent strain distributions at different displacements are compared. The experimental force−displacement curves of the two test regimes at four different temperatures and three different loading speeds are compared in Fig. 3. Then, the

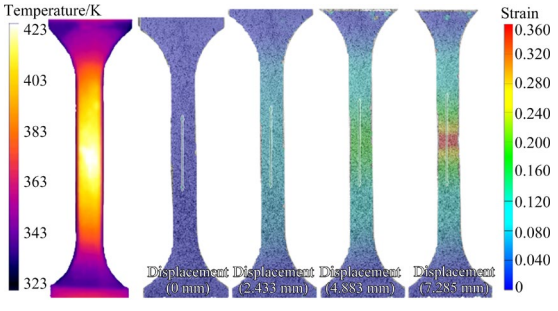

Fig. 2 Temperature and strain distribution of dogbone specimen

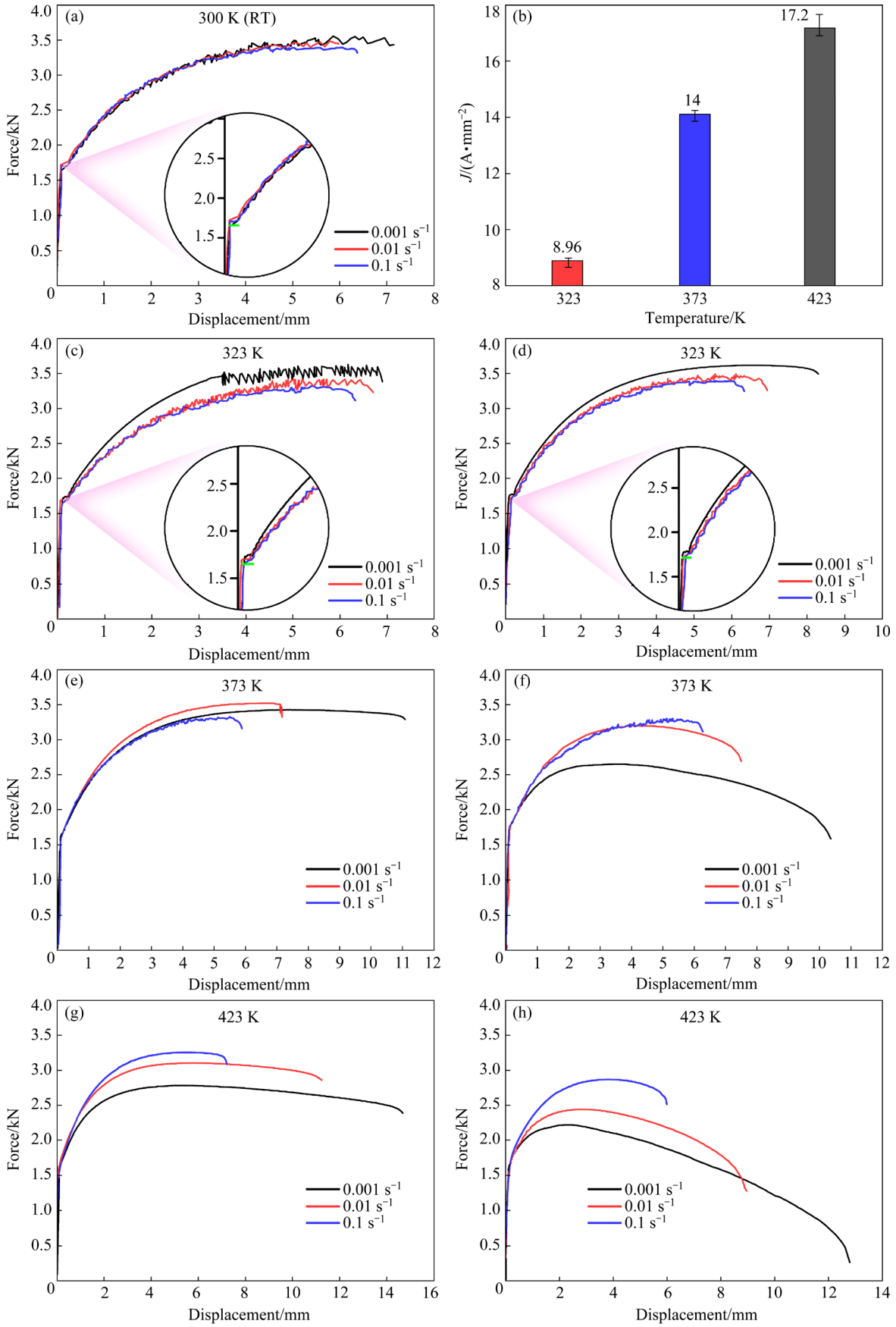

Fig. 3 Force−displacement curves of different samples at different temperatures and loading speeds (a, c−h), and current density in EAITT (b): (a) Room temperature; (c, e, g) ITT; (d, f, h) EAITT

true stress−plastic strain curves of 5182-O aluminum alloy are calculated according to the force−displacement curves before the maximum force and shown in Fig. 4. In order to achieve the corresponding initial temperature tests, the current densities are approximately adjusted to 8.96, 14 and 17.2 A/mm^2, as shown in Fig. 3(b). Repeated experiments under different loading conditions are verified and the selected one is shown below.

The Lüders platform and Portevin–Le Chatelier (PLC) effect can be clearly seen from the uniaxial tensile results of 5182-O aluminum alloy in Fig. 3. From the enlarged view of the Lüders platform in Fig. 3, it can be found that the length of the Lüders platform of the two heating methods is approximately the same when the temperature is 323 K. But the Lüders platform disappears above 373 K. It can be concluded that the acceleration effect of temperature on the diffusion of solid solution atoms and dislocation slip is more obvious in the yield platform stage than the effect of electron wind.

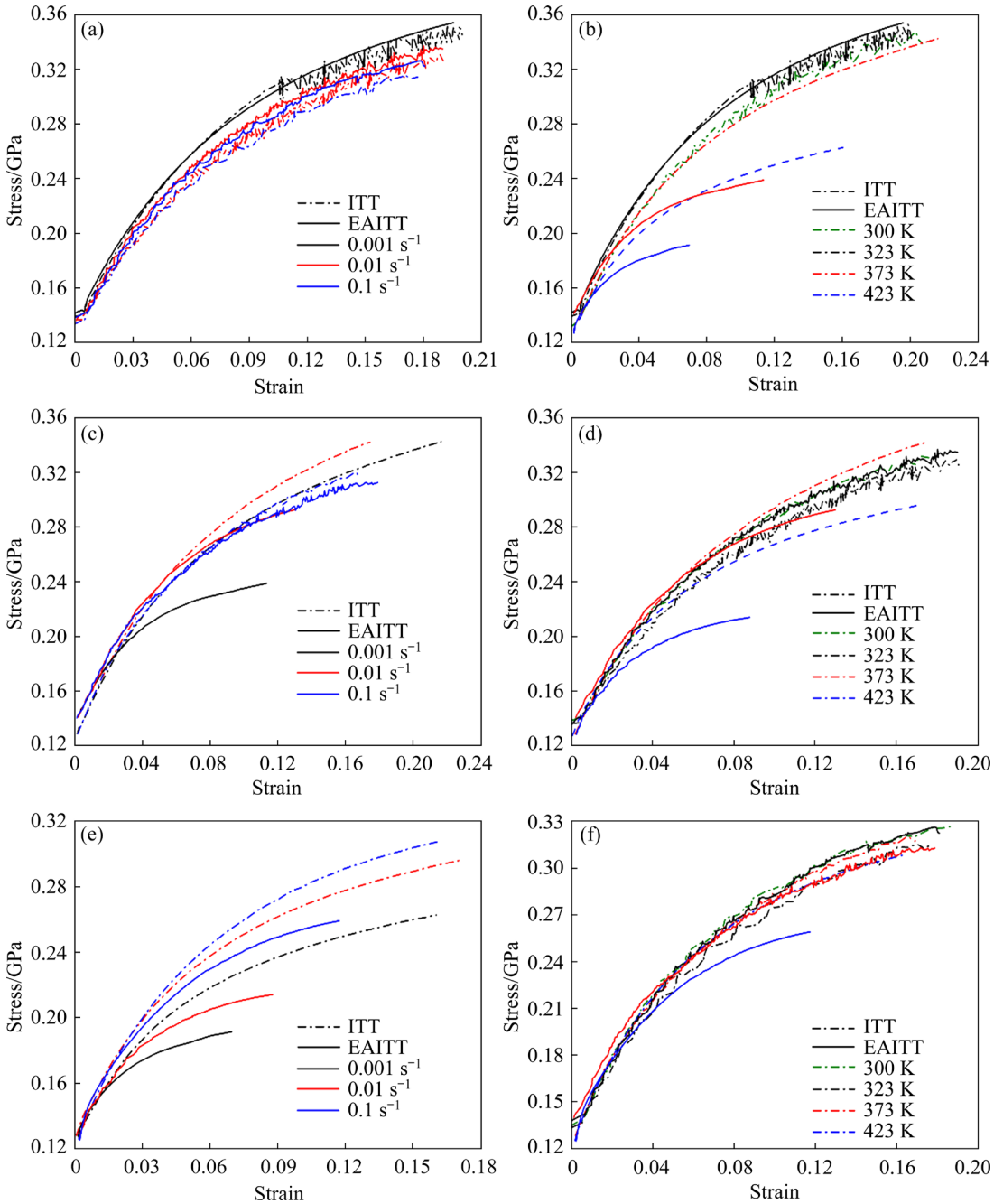

Fig. 4 Experimental stress−strain curves of samples under different conditions: (a) 323 K; (c) 373 K; (e) 423 K; (b) 0.001 s^{-1}; (d) 0.01 s^{-1}; (f) 0.1 s^{-1}

It can be found that the amplitude of the stress drop gradually increases with the increase of the strain for most of the tensile curves such as at room temperature, and the type of PLC serration is type B+C [35]. There are special cases like the ITT test at 300 K and 0.001 s^{-1}, where the front part is smooth but suddenly the stress drop is very large at a displacement of about 3.5 mm with the PLC serration of type C. The physical explanation is that the higher the density of accumulated dislocations is, the larger the scale of collective depinning occurs. But under the same condition, the curve obtained by the EAITT is smooth even under large strain. The contrasting results between the two sets of curves indicate that the electrical pulse has an independent contribution to the reduction of dislocation density. The electrical pulse promotes the stability of the plastic region and plays a dominant role in the suppression of serrated flow.

The comparison results of the true stress−strain at the same temperature are shown in Figs. 4(a, c, e). It is observed in Fig. 4(a) that the stress intensity of the 5182-O aluminum alloy measured at 323 K decreases with increasing strain rate for both test methods. The effect of electrical pulse on stress intensity is not obvious due to the small current density. This negative strain rate effect can be explained by the mechanism of dynamic strain aging (DSA) which is the dynamic interaction between mobile dislocations and solid solution atoms under specific loading conditions, such as Mg in Al−Mg based alloys. Figure 4(c) shows that the stress intensity at the strain rate of 0.01 s^{-1} is the largest in the ITT results, while the stress intensities of 0.01 and 0.1 s^{-1} are relatively close in the EAITT results. Therefore, the electrical pulse can promote the 5182-O aluminum alloy to exhibit positive strain rate effect above 373 K. Both test results show positive strain rate effect at 423 K, but the stress intensities of ITT test are generally higher under the same conditions. It is obvious that the necking strain increases with the increase of the strain rate at 423 K, indicating that high strain rate can improve the formability. In summary, the electrical pulse promotes the positive strain rate effect at low current density, and the measured stress intensity at high current density is lower than that of the ITT test.

Finally, experimental results at different temperatures under the same strain rate are compared as shown in Figs. 4(b, d, f). It can be seen from Fig. 4(b) that the softening effect of the EAITT at the strain rate of 0.001 s^{-1} is more obvious than that of the ITT test, and the change between different temperatures is larger for EAITT. The stress amplitudes at different temperatures and the strain rate of 0.1 s^{-1} do not change much in Fig. 4(f). The reason is that the slow stretching rate leads to a long acting time of the electrical pulse. The necking strains obtained by the EAITT and the ITT at 423 K with the strain rate of 0.001 s^{-1} are 0.07 and 0.16, respectively, which indicates that the large current density has a more obvious effect on the necking. It is concluded that the effect of electric pulse on softening and necking strain is stronger at low strain rate, and the effect is not obvious at high strain rate.

3.2 Microstructure

Figure 5 shows the TEM bright-field images of the dogbone specimens stretched at 423 K with different heating methods and strain rates. The dislocation is observed at the crystal boundary and inside. Dynamic recovery can be triggered easily for aluminum alloys during deformation due to their high stacking fault energy, which leads to the rearrangement and annihilation of dislocations to form well-defined dislocation cells or subgrains.

Figures 5(a, b) show dislocation distributions at different strain rates under the EAITT. It is found that the dislocation density at the strain rate of 0.1 s^{-1} is significantly larger than that at the strain rate of 0.001 s^{-1}, so the strain rate has a significant effect on the dislocation distribution. The deformation time shortens as the strain rate increases, so the dislocations do not have enough time to annihilate and rearrange. The suppressed dynamic recovery leads to the accumulation of dislocations at the crystal boundaries [36,37]. The dislocation density increases with increasing strain rate, which is consistent with the dislocation density calculated by XRD pattern in Fig. 6(b).

Moreover, dislocations tend to be parallel at high strain rates, and this phenomenon is more obvious at higher strain rates. Due to the reduction of dislocation tangles, the local concentrated deformation of the stretching process is alleviated and the plastic strength of the material is improved. In addition, it can be found that obvious Moiré patterns appear on the surface of some particles in

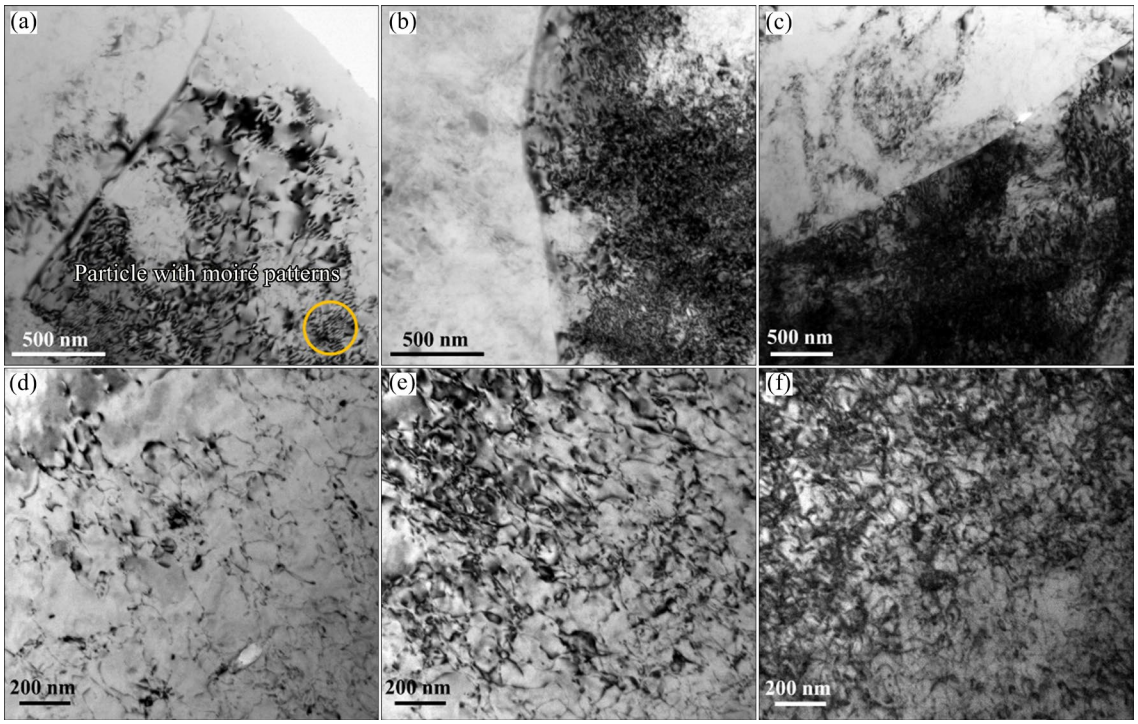

Fig. 5 TEM bright-field images of specimens stretched at 423 K with different heating methods and strain rates: (a, d) EAITT, 0.001 s^{-1}; (b, e) EAITT, 0.1 s^{-1}; (c, f) ITT, 0.1 s^{-1}

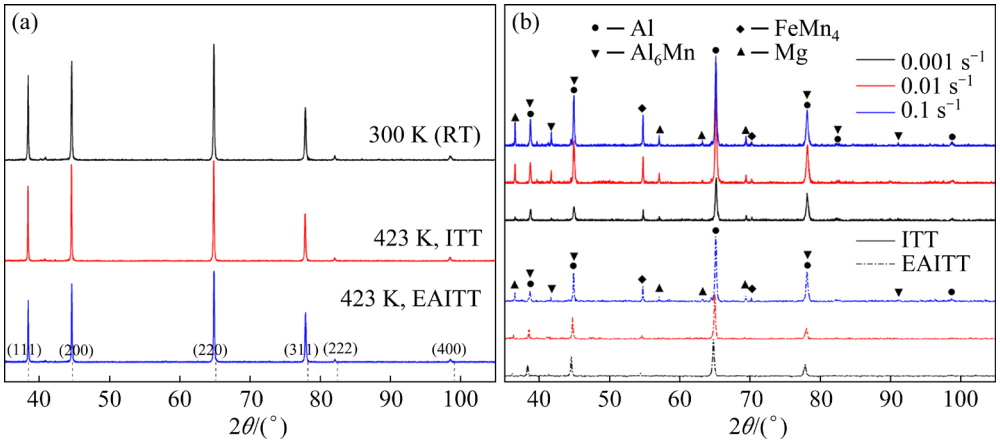

Fig. 6 XRD patterns of 5182-O aluminum alloy: (a) Before deformation; (b) After deformation

the dislocation tangles in Fig. 5(a). This may be a semi-coherent relationship caused by dislocations cutting through the particles and periodic dislocations of atoms inside the particles [38].

From the comparison of the results of Figs. 5(b, c), it is found that the dislocation density of the EAITT is lower than that of the ITT at the same strain rate. High density dislocation tangles occur near crystal boundaries during ITT in an environmental cabinet. This indicates a higher frequency and magnitude of interactions between solute atoms and mobile dislocations. The enhancement of solute atomic diffusion induced by the electric current thus leads to an increase in mobile dislocation locking, which provides clear evidence for the suppression of the PLC effect at relatively low temperatures [39].

The XRD patterns (Fig. 6(a)) of the 5182-O aluminum alloy before deformation by different heating methods show sharp diffraction peaks of aluminum (PDF: No. 04-0787). XRD relative intensities of major peaks show a significant decreasing trend with the increase of temperature. It is obvious from the comparison that the relative

intensities obtained by the EAITT at 423 K are significantly lower than those obtained by the ITT. Since the peak width of the EAITT is lower than that of the ITT at the corresponding temperature, the independent contribution of current to the reduction of dislocation density is confirmed [40]. The precisely scanned XRD patterns (Fig. 6(b)) of the specimens after deformation exhibit weak diffraction peaks for Mg (PDF: No. 35-0821), Al_6Mn, and $FeMn_4$ precipitates (PDF: No. 39-0952, 03-1180, respectively). At the same temperature and strain rate, the relative intensities of EAITT are significantly lower than those of ITT. Precipitates in supersaturated solid solutions are suppressed due to the electromigration effect induced by the electric current, thereby weakening the interaction between precipitated phase and dislocations [39]. Moreover, the relative intensities of EAITT at 0.1 s^{-1} are significantly higher than those at 0.001 s^{-1} at the same temperature. This is due to the fact that as the strain rate increases, the drift electrons in the metal have shorter time under the action of the current, resulting in a more pronounced effect at lower strain rates.

The Al_6Mn dispersoids precipitate after tensile deformation of the sample under different conditions, which is confirmed in the electron diffraction patterns of Fig. 7(c) [41]. The distributions of different elements (Al, Mn, Mg, Fe, and Cu) obtained by EDS mapping of the 5182-O aluminum alloy precipitates tested by EAITT at 423 K are shown in Figs. 7(e–i). This semi-quantitative or qualitative method of compositional analysis by EDS is used to characterize the microstructure. It can be found that the segregation of Al and Mn is accompanied by the depletion of Mg. This indicates the existence of Al-rich and Mn-rich precipitates in the sample, and the molar ratio is close to 6:1. At the same time, it is accompanied by the precipitation of a small amount of Fe and Cu. In conclusion, the dislocation density obtained by EAITT is lower than that obtained by ITT at the same initial temperature, and the dislocation density increases with the increase of the strain rate. This is consistent with the experimental results in Fig. 3, because dislocation density is positively correlated with deformation resistance.

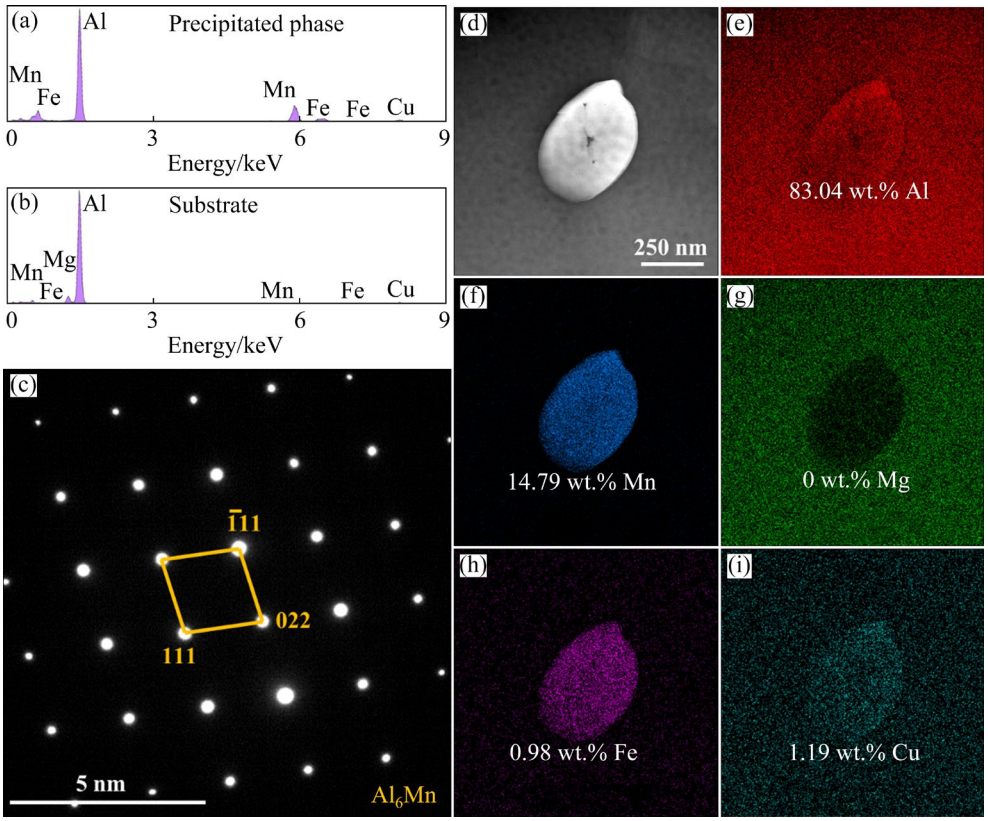

Fig. 7 Characterization of 5182-O aluminum alloy after EAITT or ITT: (a, b) EDS results of precipitated phase and substrate, respectively; (c) Selected area electron diffraction pattern with electron beam parallel to $\langle 001 \rangle_{Al}$ zone axis; (d) TEM image; (e, f, g, h, i) EDS mappings for distribution of Al, Mn, Mg, Fe and Cu, respectively

To further determine the phases present in the 5182-O aluminum alloy, TEM samples are prepared near the fracture tip of the tensile specimen subjected to 17.2 A/mm^2 with a strain rate of 0.1 s^{-1}. The TEM images and the corresponding EDS maps in Fig. 8 show that there are some phases with the size of tens of microns in the matrix. It can be seen that the number of Al_6Mn phases is more than that of Mg and $FeMn_4$ phases, which is consistent with XRD results in Fig. 6.

Figures 9(a) and (b) show the EBSD microstructures of the undeformed region and the fracture location by EAITT at 423 K and a strain rate of 0.1 s^{-1}, respectively. The random orientation distribution can be observed in Figs. 9(a) and (b), which shows that the grains elongate in the loading direction with the increase of tensile strain. The microstructure evolution during material deformation is further reflected by texture property. The texture evolution of 5182-O aluminum alloy

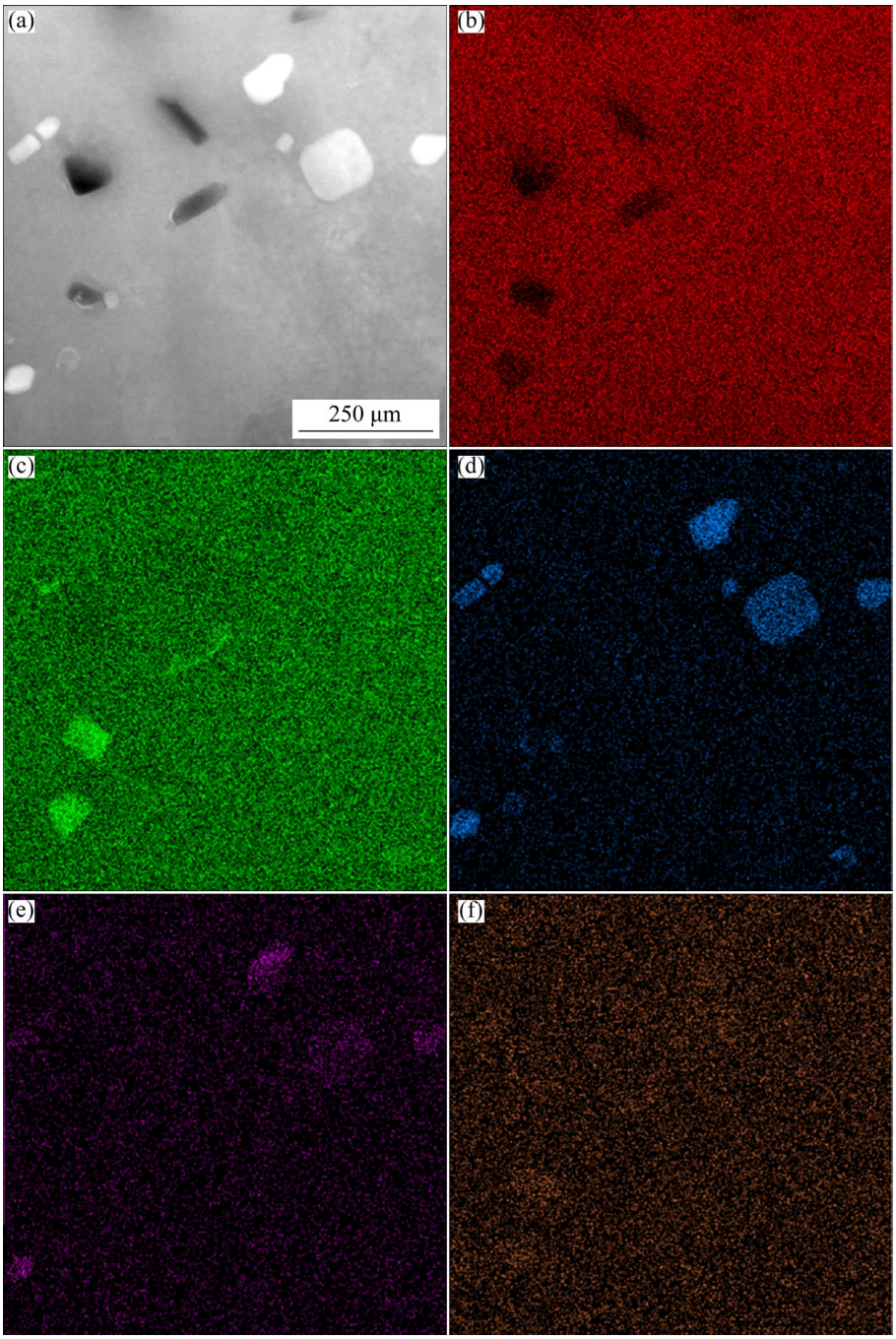

Fig. 8 TEM image (a) and element distributions of Al (b), Mg (c), Mn (d), Fe (e) and Cu (f) obtained by EAITT test at 423 K and strain rate of 0.1 s^{-1}

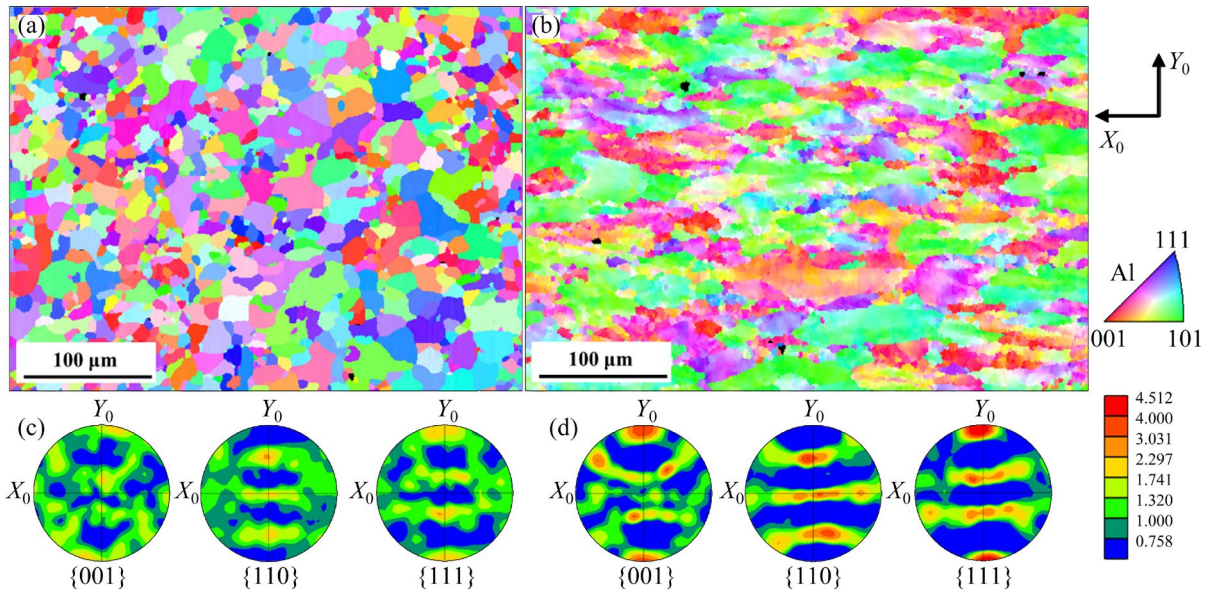

Fig. 9 EBSD microstructures (a, b) and pole figures (c, d) of 5182-O aluminum alloy heated to 423 K with strain rate of 0.1 s^{-1} by EAITT: (a, c) Undeformed region; (b, d) Fracture location

before and after plastic deformation is shown in Figs. 9(c) and (d), respectively. The random texture is observed in the undeformed state in Fig. 9(c), and the texture is found to be enhanced after tensile deformation in Fig. 9(d) where the maximum pole density increases to 4.512.

Figure 10 shows the SEM fractographs of the tensile specimens at 423 K under the three loading conditions. The fracture surface in Fig. 10(c) is nominally flat compared to the other two fracture surfaces, and there is an obvious necking at the fracture of the specimen in Fig. 10(b). Mixed dimples and tearing edges in the three tensile specimens at a finer scale indicate ductile fracture. The dimples are generally produced by the nucleation, growth, and coalescence of micro-voids, and tearing edges ought to be formed by the coalescence of micro-voids or the connection of micro-voids. The fracture morphology in Fig. 10(a) shows many blade-type edges and coalescent dimples. The dimples in Fig. 10(b) are larger and deeper than those in Fig. 10(a) and tend to coalesce. The identifiable tearing edges indicate that electroplasticity facilitates the diffusion and transfer of dimples, whereby the expansion of microscopic dimples under this deformed condition promotes high elongation. Figure 10(c) shows the fracture morphology of the sample heated to 423 K by EAITT at a strain rate of 0.001 s^{-1}. It can be found that the increase of the strain rate can increase the number of dimples and reduce their size and depth from the comparison results of Figs. 10(c) and (e). The enhanced tearing edges and flat fracture surfaces mean that increasing the strain rate reduces necking and elongation. In addition, the second phase particles are easily found inside some dimples observed under magnification, and these active sites for void nucleation adversely affect ductility.

3.3 Calculation of dislocation density

The broadening of the full width at half maximum (FWHM) in the XRD spectrum is widely used to characterize the dislocation density of peak-aged alloys. The dislocation density of the sample under different conditions is calculated by the modified Williamson−Hall (MWH) equation according to FWHM [42], as shown below:

$$\Delta K \approx \frac{\gamma}{D} + \left(\frac{\pi M_1^2 b^2}{2}\right)^{1/2} \rho^{1/2} K\overline{C}^{1/2} + o\left(K^2\overline{C}\right) \quad (1)$$

where $\Delta K(=\beta\cos\theta/\lambda)$ is the peak width (β is the FWHM of diffraction peak, λ(=0.15405 nm) is the wavelength, and θ is the diffraction angle); D is the crystallite size; b is the magnitude of the Burgers vector (0.286 nm); ρ is the dislocation density; γ is the shape factor and takes the value of 0.9 when the

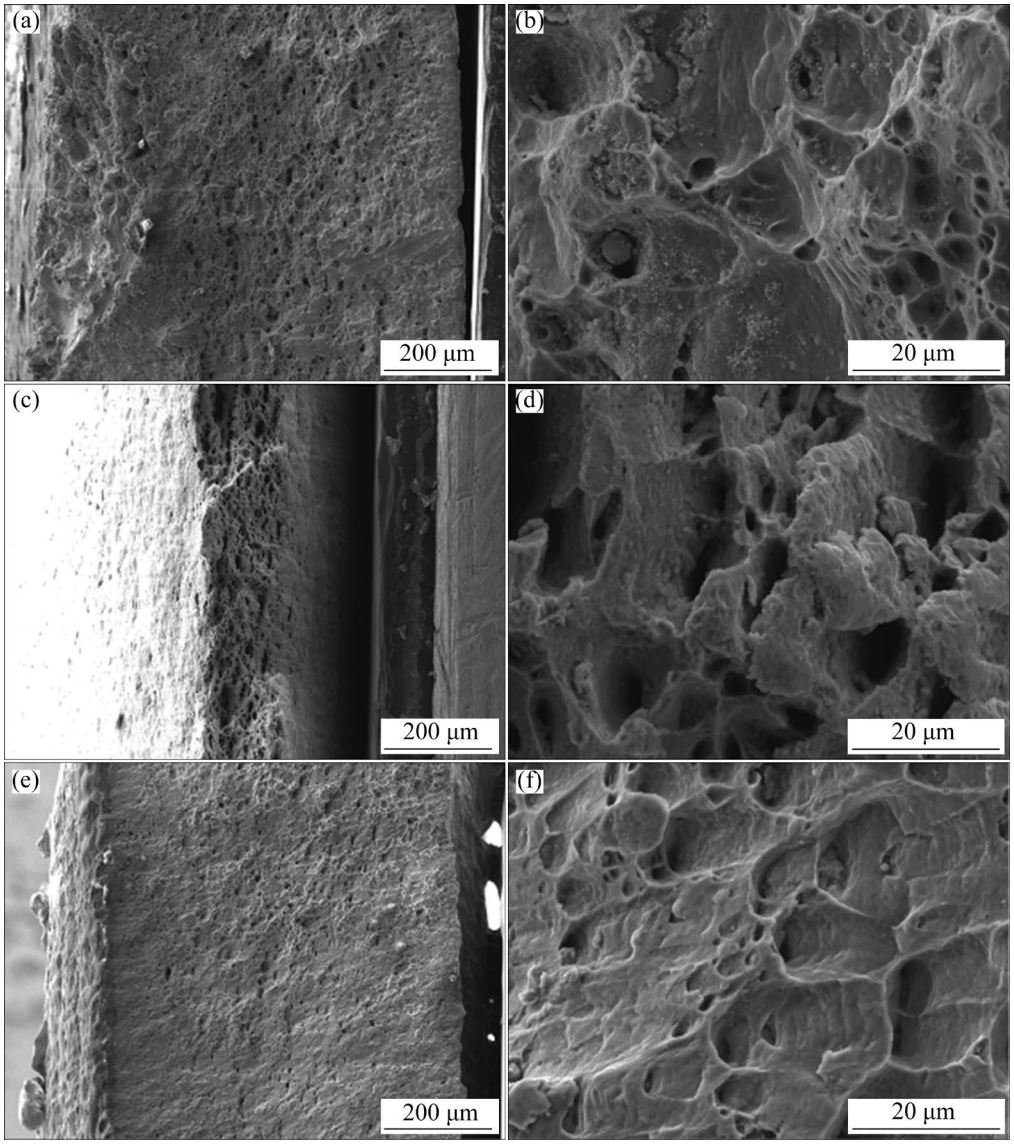

Fig. 10 SEM fractographs of tensile specimens at 423 K under different loading conditions: (a, b) ITT, 0.001 s^{-1}; (c, d) EAITT, 0.001 s^{-1}; (e, f) EAITT, 0.1 s^{-1}

FWHM method is used in the analysis [43]; M_1 is a dimensionless constant with a value between 1.0 and 2.0 in the deformed material and is known as the dislocation distribution parameter [38]; K is the magnitude of diffraction vector and is defined as $K=2\sin\theta/\lambda$; $o(K^2\overline{C})$ represents the deviation from this approximation; $\overline{C}$ is the dislocation contrast factor of cubic crystal materials as a function of the Miller indices and can be determined by applying the method given below [44]:

$$\overline{C}=\overline{C}_{h00}(1-qH^2) \tag{2}$$

where $\overline{C}_{h00}$ is the average contrast factor corresponding to the (h00) reflection; q is a proportional coefficient that depends on the elastic constant of the material and the ratio of edge dislocation and screw dislocation. H^2 is represented as [45]

$$H^2=(h^2k^2+k^2l^2+h^2l^2)/(h^2+k^2+l^2)^2 \tag{3}$$

where h, k, and l are the Miller indices of each peak. Equations (1) and (2) are combined to obtain the following equation [42]:

$$(\Delta K-\gamma/D)^2/K^2\cong\overline{C}_{h00}(1-qH^2)(\pi M_1^2b^2\rho)/2 \tag{4}$$

The proportional coefficient q is equal to the inverse ratio of the slope to the intercept of the $(\Delta K-\gamma/D)^2/K^2$ vs H^2 curve. For aluminum alloy, the q value changes between 0.33 and 1.31, and the $\overline{C}_{h00}$ values change between 0.182 and 0.199 [46].

Then, ΔK vs $K\overline{C}^{1/2}$ calculated according to the above equations can be linearly fitted according to Eq. (1), as shown in Fig. 11(a). The values of $bM_1\sqrt{\pi\rho/2}$ are equal to the slope. Finally, the calculated dislocation density values are shown in Fig. 11(b).

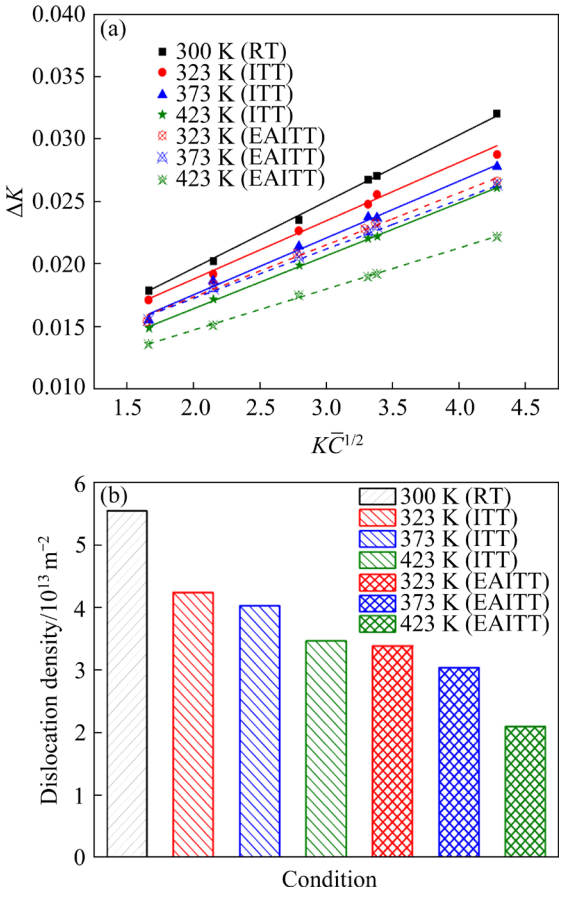

Fig. 11 Linear fitting results of ΔK versus $K\overline{C}^{1/2}$ (a) and calculated dislocation densities (b) at different temperatures

It is evident from Fig. 11 that the initial dislocation density in the specimen decreases with the increase of temperature, but the effect of electric pulse on the initial dislocation density is more obvious. The dislocation density decreases significantly with the increase of current density, and the dislocation density at 423 K reduces to 2.09×10^{13} m^{-2} for EAITT test. It should be noted that the values of some parameters, such as M_1, are difficult to obtain accurately, so the actual dislocation density is only a rough estimate. However, the results indicate that the annihilation of dislocations is promoted by the electromigration effect and Joule heating induced by the electrical pulse [47].

4 Evaluation and numerical simulation of three typical constitutive models

4.1 Constitutive model

4.1.1 MKM model based on dislocation density

Work hardening and dynamic recovery softening lead to the rearrangement and annihilation of dislocations during thermal deformation of metals. The mechanical response is independently related to the evolution of the microstructure [48], so the accumulation of dislocations can increase the ability to working-harden while the recovery of dislocations increases plastic instability. The average dislocation density ρ, as a structure-dependent variable, describes the dynamic hardening behaviors of metals according to different loading conditions [6]. The Kocks−Mecking model based on dislocation−dislocation interactions is applied to describing the flow stress of metals during plastic deformation. In previous studies, the generalized Kocks−Mecking model was used to describe the stress−strain curves obtained from solution-treated, naturally aged, and current-assisted samples. TIWARI et al [49] extended this model to describe the effect of electrical pulse, and there is the following relationship between the flow stress (σ) and ρ:

$$\sigma=M\alpha Gb\sqrt{\rho}(\dot{\varepsilon}/\dot{\varepsilon}_0)^{1/m} \tag{5}$$

where M is the Taylor factor, G is the shear modulus (MPa), $\dot{\varepsilon}$ is the strain rate, and m is the exponent describing the strain rate dependence, and $\dot{\varepsilon}_0$ and α are material constants of work hardening. The evolution of dislocation density is given by

$$\frac{\mathrm{d}\rho}{\mathrm{d}\varepsilon}=M\left(K_1\sqrt{\rho}-K_2\rho\right) \tag{6}$$

where K_1 and K_2 are coefficients to describe Stage II and Stage III work hardening, respectively.

Since dynamic recovery in metals during State III recovery is rate dependent, the coefficient K_2 can be modelled as follows:

$$K_2=K_{20}\left(\dot{\varepsilon}/\dot{\varepsilon}_0\right)^{-1/n} \tag{7}$$

where K_{20} and n are material constants to describe the temperature dependence.

The material constants α and n are considered to be temperature and strain rate dependent. The above parameters should vary with current density

(J) in the EAITT due to the effect of the electrical pulse on the strain rate as follows [50]:

$$\alpha=\alpha_0\beta_1\left\{\dot{\varepsilon}^{\beta_2}T^{\beta_3}+\frac{\beta_4}{\beta_1}J^{\beta_5}\right\} \tag{8}$$

$$n=\beta_6\left\{T^{\beta_7}+\frac{\beta_8}{\beta_6}J^{\beta_9}\right\} \tag{9}$$

where α_0 and β_1−β_9 are fitting coefficients. K_2 and α adjust the stress variation with temperature and strain rate, and β embodies the temperature-decoupled electroplastic effect.

The fixed hardening rate for Stage II hardening is defined by the constant K_1. The constant K_2 describes the dynamic recovery or annihilation of dislocations in Stage III hardening. Equation (6) can be directly integrated to yield

$$\sqrt{\rho}=\left(\sqrt{\rho_0}-\frac{K_1}{K_2}\right)\exp\left(-\frac{MK_2}{2}\varepsilon\right)+\frac{K_1}{K_2} \tag{10}$$

Substituting Eq. (10) into Eq. (5)

$$\sigma=M\alpha Gb\left(\frac{\dot{\varepsilon}}{\dot{\varepsilon}_0}\right)^{1/m}\left(\left(\sqrt{\rho_0}-\frac{K_1}{K_2}\right)\exp\left(-\frac{MK_2}{2}\varepsilon\right)+\frac{K_1}{K_2}\right) \tag{11}$$

where ρ_0 is the initial dislocation density when ε=0. The main advantage of the MKM model is that the parameters are directly related to the deformation mechanism. It should be emphasized that the MKM model takes into account the electroplastic effect on flow stress through the variables n and α, respectively. The coefficients of the MKM model are calibrated as listed in Table 1.

4.1.2 Newly proposed MLH model

Modelling the current-assisted flow stresses remains challenging because of the differences in the action mechanisms in the EAITT and ITT. In addition, the 5182-O aluminum alloy exhibits a slightly negative strain rate effect at room temperature due to DSA, while the strain rate effect becomes positive with increasing temperature. For the highly nonlinear hardening behaviors, the phenomenological constitutive model needs to be constructed to reflect the contribution of different effects to the flow stress. CAO et al [21] considered Joule heating and strain rate effect, dynamic strain aging and electronic wind effect in the model. The Lim−Huh (LH) model [51], which can accurately express the strain rate effect, is additively extended to the MLH model to describe the flow stress under different current densities:

$$\sigma(\varepsilon,\ \dot{\varepsilon},\ T)=\lambda_{\mathrm{RK}}[\sigma_{\mathrm{lh}}(\varepsilon,\ \dot{\varepsilon},\ T)+\sigma_{\mathrm{ns}}(\dot{\varepsilon},\ T)+\sigma_{\mathrm{ew}}(J)] \tag{12}$$

The Young's modulus ratio (λ_{RK}) is neglected due to little variation over the test temperature range. The first term σ_{lh} represents the combined contribution of strain, strain rate, and temperature to the flow stress, and the σ_{ns} and σ_{ew} represent the DSA and electronic wind effects, respectively. σ_{lh} takes the form of LH model as follows:

$$\sigma_{\mathrm{lh}}=[\sigma_{\mathrm{r}}(\varepsilon)]\cdot[\sigma_{\dot{\varepsilon}}(\varepsilon,\dot{\varepsilon})]\cdot[\sigma_T(T,\dot{\varepsilon})]=A(\varepsilon+\varepsilon_0)^n\cdot\left[\frac{1+q(\varepsilon)\dot{\varepsilon}^{p(\varepsilon)}}{1+q(\varepsilon)\dot{\varepsilon}_{\mathrm{r}}^{\ p(\varepsilon)}}\right]\cdot\left[1-\left(\frac{T-T_{\mathrm{r}}}{T_{\mathrm{m}}-T_{\mathrm{r}}}\right)^{m(\dot{\varepsilon})}\right] \tag{13}$$

where A and n are the strain hardening coefficients, $q(\varepsilon)=q_1/[(\varepsilon+q_2)^{q_3}]$, $p(\varepsilon)=p_1/[(\varepsilon+p_2)^{p_3}]$, $m(\dot{\varepsilon})=m_1+m_2\ln(\dot{\varepsilon}/\dot{\varepsilon}_{\mathrm{r}})$, $\dot{\varepsilon}>\dot{\varepsilon}_{\mathrm{r}}$ and $T_{\mathrm{r}}\le T\le T_{\mathrm{m}}$ (q, q_2, q_3, p_1, p_2, p_3, m_1, and m_2 are material constants; T_{r} is the room temperature, and T_{m} is the melting point).

DSA is the result of dynamic pinning/unpinning caused by the interaction of moving solute atoms and dislocations in the metal. The occurrence of DSA largely depends on the difference

Table 1 Material coefficients of constitutive models

Model	M	α_0	G/MPa	b/nm	m	K_1	K_{20}	$\dot{\varepsilon}_0$/s^{-1}
MKM	3	0.8078	27000	0.286	−0.0537	136407	22.21	1.47×10^{-14}
Model	β_1	β_2	β_3	β_4	β_5	β_6	β_7	β_8	β_9
MKM	7.909	0.0410	0.1742	-1.97×10^{-12}	−74.94	2.6185	0.5057	0.0035	3.0659
Model	A	ε_0	n	q_1	q_2	q_3	p_1	p_2	p_3
MLH	514.2	0.0052	0.3033	0.0557	−0.0011	0.2099	3.55×10^{-11}	4.81×10^{-19}	2.7875
Model	m_1	m_2	σ_0^{ns}	$\dot{\varepsilon}_{\mathrm{trans}}$	D_3	$\dot{\varepsilon}_{\max}$	M_{Tavlor}	b/nm	K_{ew}
MLH	0.927	0.2141	2.3261	76.58	0.0089	10^6	2.5	0.286	−0.0644

between the waiting time of the dislocations at the local obstacle and the time for diffusion of the solutes to the mobile dislocations [52]. Therefore, it is important for modelling that the flow behavior should be limited by strain rate and temperature. Semi-physical formulation [53] is used to model the σ_{ns} in the equation for combined accuracy and practicality.

$$\sigma_{ns}\left(\dot{\varepsilon},T\right)=\sigma_0^{ns}\cdot\left[\lg\left(\frac{\dot{\varepsilon}_{trans}}{\dot{\varepsilon}}\right)\right]\cdot \left[1-D_3\left(T_m/T\right)\lg\left(\dot{\varepsilon}/\dot{\varepsilon}_{max}\right)\right] \tag{14}$$

where σ_0^{ns} is the reference stress drop due to DSA, D_3 is the interaction coefficient between strain rate and temperature, $\dot{\varepsilon}_{trans}$ is the transition strain rate between positive and negative strain rate effects, and $\dot{\varepsilon}_{max}$ is the maximum allowable strain rate of the material.

The electron−dislocation interactions due to the electron wind are considered in the last stress component σ_{ew}. The moving electrons are assumed to promote the slip of dislocations directly through momentum transfer, and the relationship between electron wind stress and current density is as follows.

$$\sigma_{ew}=\frac{M_{Taylor}}{b}K_{ew}J \tag{15}$$

where K_{ew} is the electron wind coefficient, and M_{Taylor} is the Taylor orientation factor. The coefficients of the calibrated MLH model are shown in Table 1.

4.1.3 Neural network model

Machine learning was applied in EAP to evaluate the influence of electroplastic effect on flow stress and plasticity. The structure diagram of the ANN model is shown in Fig. 12. The strain, temperature and strain rate are used as inputs to reflect the coupled effects of strain hardening, temperature softening and strain rate hardening. It is worth noting that different current densities are input in order to differentiate the effect of electrical pulse on EAITT and ITT. In order to obtain high-quality input samples, appropriate mathematical transformations are performed to more accurately capture the characteristics of the data. Therefore, the corresponding ranges of the four inputs of ε, $\dot{\varepsilon}$, T and J in Fig. 12 are [0, 0.4], [lg 300, lg 423], [lg 0.001, lg 0.1], and [ln(e^0+1), ln($e^{17.2}$+1)], respectively.

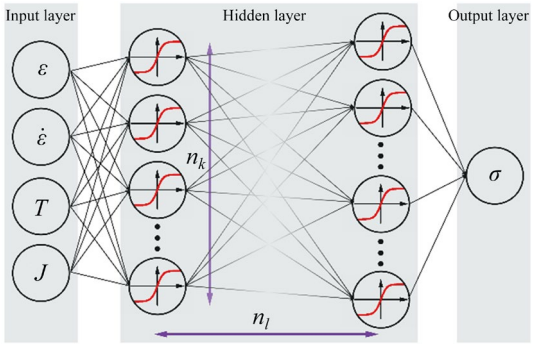

Fig. 12 ANN model architecture

It is necessary to comprehensively consider the structure and parameters of the ANN model in order to achieve the optimal combination of prediction accuracy and numerical calculation efficiency. In previous work [33], it is confirmed that the computation time of the numerical simulation is positively correlated with the number of neurons (the sum of weights and thresholds). The number of neurons in the first hidden layer has a dominant effect on the prediction accuracy under the same number of parameters. The number of neurons in the first layer less than the number of input variables may lead to the loss of input information, while too many neurons increase the burden of numerical simulation. The prediction error can reach a plateau after the inflection point, and the prediction accuracy is not improved significantly with the complexity of the network structure. In addition, the prediction error of the ANN optimized by the PSO algorithm can quickly reach a lower level after the structure of the network is determined. Finally, the single-hidden-layer PSO−BP network with 20 neurons is chosen to fully exploit its potential of high prediction accuracy and low computation time. The ANN model with a structure of 4×20×1 has a total of 121 parameters and the combination of activation functions is tansig + purelin. The number of epochs is adjusted to 3000, and the iterative update is performed by the Levenberg−Marquardt algorithm with a learning rate of 0.01 and a momentum of 0.9.

There are many input variables and the strain rate interval is large, so it is difficult to ensure that the prediction results beyond the experimental values are also satisfactory only based on the limited experimental data. The experimental data are enriched by the analytical model to provide

large data samples for ANN training. Due to the flexible power-law relationship between strain and strain rate in Ford model, it is found that the prediction accuracy is relatively high by comparing with the LH and other models. Therefore, the Ford model is selected to calibrate and enrich the experimental values. Then, two sets of virtual experimental results are generated by interpolating between each set of strain rates, which ensures smooth surfaces and reasonable prediction results in the presence of many surface intersections. The expression for the Ford model is as follows:

$$\sigma(\varepsilon,\dot{\varepsilon})=A_1+B\varepsilon+C[1-\exp(-D\varepsilon)]^E+F(\dot{\varepsilon}^{G_1}-\dot{\varepsilon}_0^{G_1}) \tag{16}$$

where A_1, B, C, D, E, F and G_1 are the calibrated parameters. Four sets of curves are interpolated among the three sets of strain rates, and a total of 28 sets of curves are obtained by interpolating the seven surfaces calibrated by the Ford model. The calibrated 2296 virtual experimental points are used to enrich the experimental data, and finally a total of 7762 sample data including experimental data are obtained. Then, 6985 data points accounting for 90% of the sample data are selected as the training set, and the remaining 10% are used as the test set to evaluate the predictability of the model. The speed and position of the particles in the PSO algorithm are iteratively updated until the ANN model training reaches the target error level.

4.2 Calibration of hardening curves

Figures 13 and 14 reflect the degree of agreement between the predicted surfaces of the constitutive models and the experimental results represented by the red solid symbols at different strain rates and temperatures. From the overall prediction results in Fig. 13, it can be seen that the predicted surfaces are relatively smooth and the trend reflects the strain hardening effect. Both the MKM model and the MLH model describe the thermal softening effect, but the predicted surfaces are relatively monotonic and rigid. The intersection of two colors on the surfaces predicted by ANN model indicates its high flexibility. The strain of 0.03 corresponds to the highest stress by EAITT at 373 K among different experiments with a strain rate of 0.01 s^{-1}, which is exactly reflected by the convexity of the surface predicted by the ANN model. Therefore, the ANN model can adjust the surfaces according to the experimental stress amplitudes and the predictions are still smooth between different strain rates. The RMSE predicted by the ANN model is only 1.9676. The prediction errors of the MKM and MLH models are 14.7915 and 14.2207, respectively, which are 7.5 times that of the ANN model. The three models are compared separately at each temperature, which can clearly express the prediction of the trend under large strain and the prediction results of the intermediate strain rate not to be covered by the experiment.

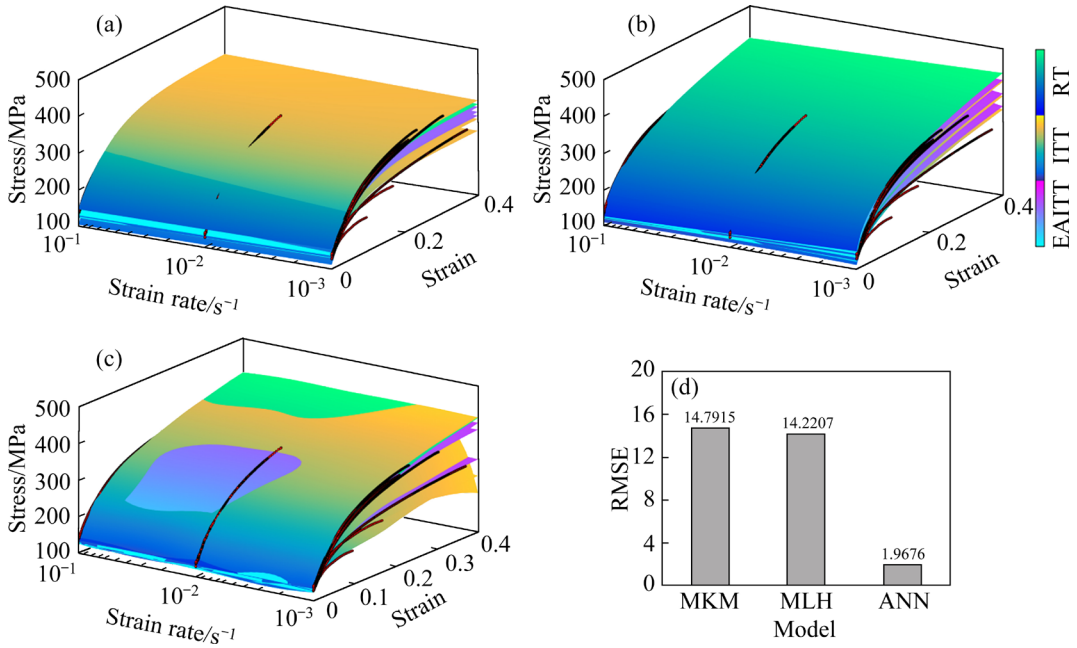

Fig. 13 Comparison between calculated flow stress and experimental data: (a) MKM model; (b) MLH model; (c) ANN model; (d) RMSEs of three models

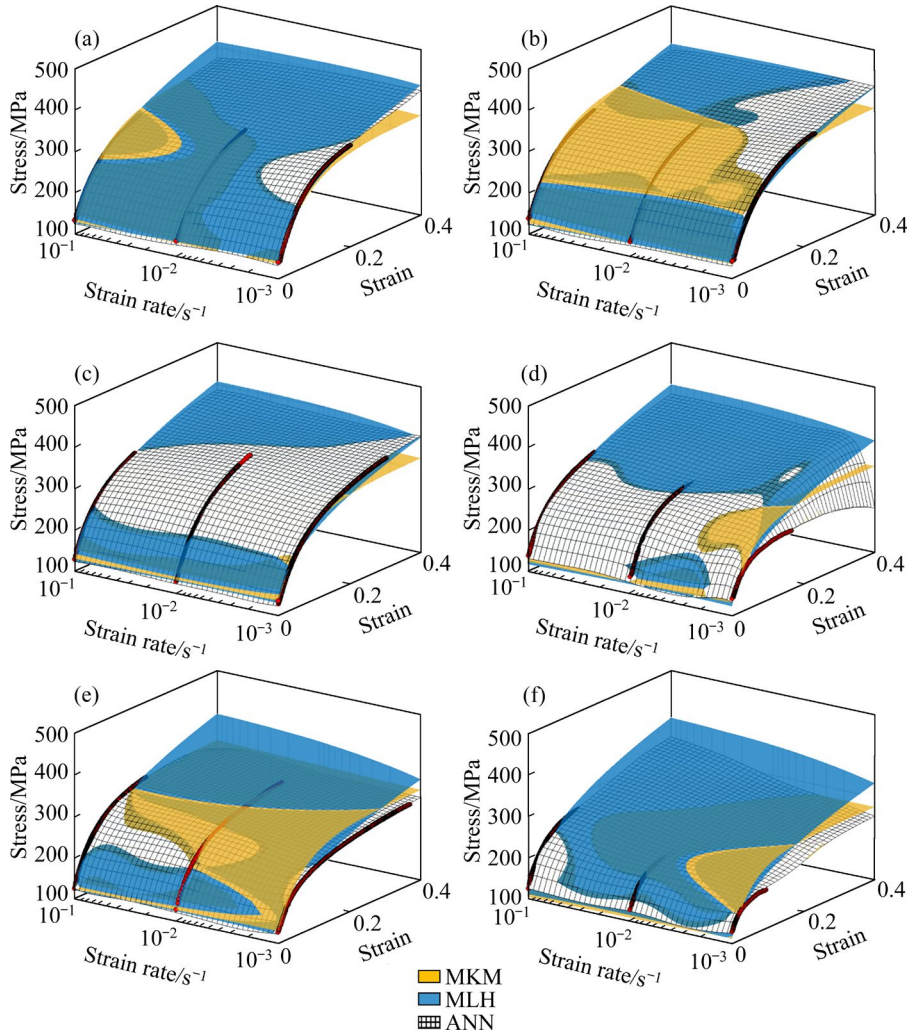

Fig. 14 Calibration results of three models at same temperature for ITT (a, c, e) and EAITT (b, d, f): (a, b) 323 K; (c, d) 373 K; (e, f) 423 K

Figure 14 shows the prediction errors of the three models and the calibration results at each temperature, respectively. There are a lot of overlaps between the three models for small strains, but it can be clearly seen that only the ANN model can accurately calibrate the hardening curve under large strains, especially the results at 423 K by EAITT. For the stresses obtained by EAITT at 373 K, there is a large difference at different strain rates, which can only be calibrated by ANN model. The ANN model can accurately reflect different hardening responses measured and all the predicted surfaces have no additional peaks or troughs outside the experimental data.

4.3 Numerical prediction of force−displacement curves

The MKM, MLH and ANN models are implemented in the commercial software Abaqus/Explicit to perform numerical simulations under different experimental conditions. A quarter model of the dogbone specimen is applied to saving running time due to the symmetry of the boundary conditions. It is assumed that the temperature remains constant throughout the simulation depending on the employment of first-order solid elements (C3D8R from Abaqus library). The comparison between the experimental results and the force displacement curves of the dogbone extracted by numerical simulations are shown in Figs. 15 and 16. It is found that the characteristics of the three models are relatively obvious. The MKM model is based on the description of dislocation−dislocation interactions, so the predictions of large dislocation densities resulting from the strain rate of 0.1 s^{-1} is the most accurate. The prediction results of the

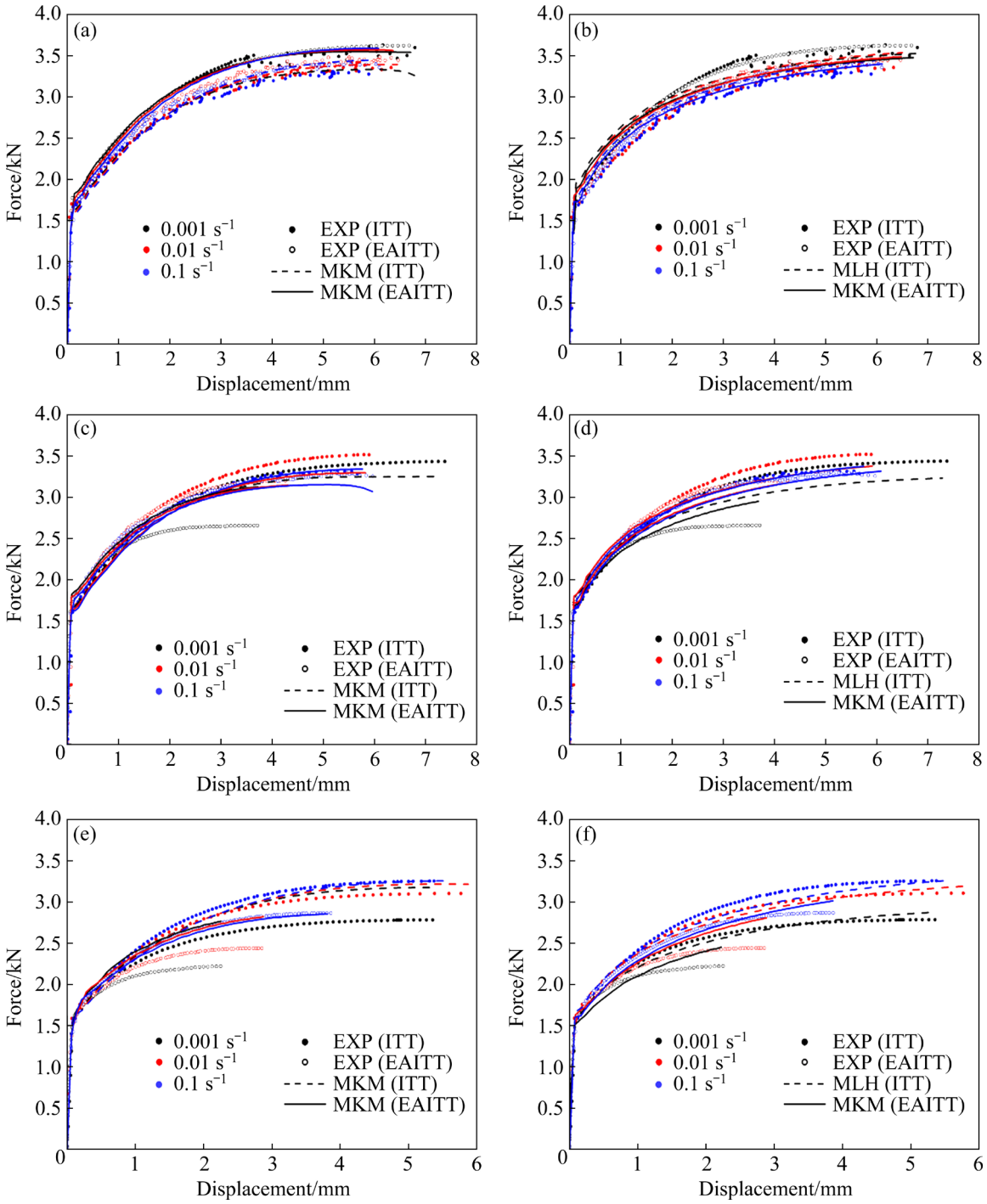

Fig. 15 Comparison of numerical simulation results of MKM and MLH models with experimental results (EXP) for dogbone specimens: (a, b) 323 K; (c, d) 373 K; (e, f) 423 K

MKM model for low strain rates are unsatisfactory, especially for the prediction results of 0.001 s^{-1} under the EAITT which are very different from the experimental values. The MLH model can reflect the general trend of each set of force−displacement curves, but most of the simulation results have a certain deviation from the experimental values. Good prediction results are attributed to the fact that the variation range of stress with different strain rates is relatively small at 323 K, but the large variation of stress amplitude leads to a large deviation at 423 K. It can be seen from Fig. 15(b) that the force−displacement curve with a strain rate of 0.001 s^{-1} is above the curve with a strain rate of 0.1 s^{-1} under the same heating mode, so the MLH model can slightly capture the negative strain rate

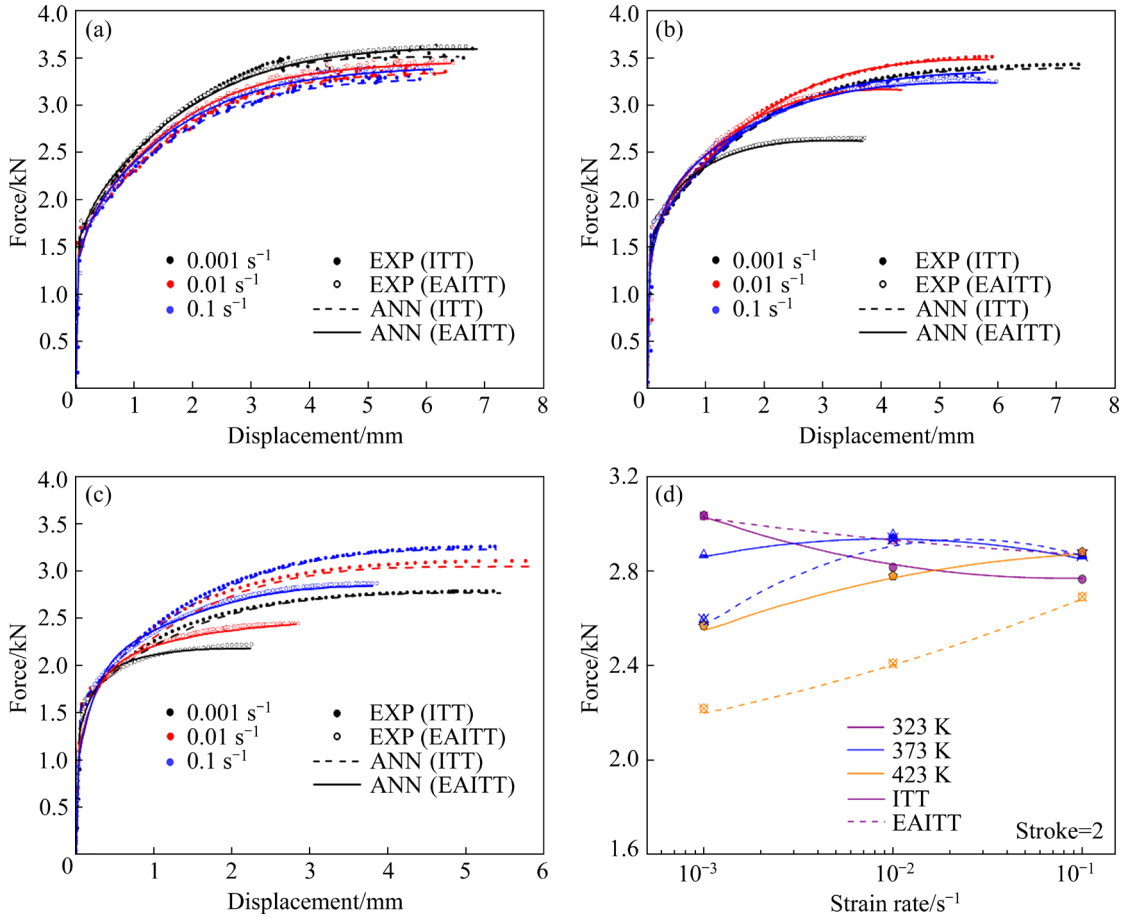

Fig. 16 Force−displacement curves predicted by ANN model for dogbone specimen: (a) 323 K; (b) 373 K; (c) 423 K; (d) Extracted force at displacement of 2 mm as function of strain rate

effect of 323 K. Even though the overall calibration errors of the two models are roughly the same, the MLH model that directly considers the coupling effects of different factors is more flexible and applicable.

The prediction results in Fig. 16 show that the calibration accuracy of the ANN model is obviously the best. It can accurately simulate the coupling effects of various effects and highly nonlinear special phenomena, such as the negative strain rate effect at 323 K, the maximum stress for the EAITT at 0.1 s^{-1} and the ITT at 0.01 s^{-1} and 373 K, and positive strain rate effects at 423 K. Different current densities are used as inputs to reflect the difference between EAITT and ITT, and the nonlinear results can be clearly distinguished and accurately predicted. In addition, computing efficiencies are compared under the same parameter settings and computer configuration (AMD Ryzen 7 4800HS with Radeon Graphics 2.90 GHz; 8.00 GB RAM; 4 CPUs for all the simulations). It is found that taking the EAITT at a strain rate of 0.01 s^{-1} and 373 K as an example, the MKM and MLH models take 3.12 min while the ANN model takes 10.45 min. The calculation time of the ANN model is roughly 3.35 times that of the analytical models, which is within the acceptable range compared to the irreplaceable prediction accuracy.

Figure 17 visually shows the comparison between the prediction results of the three models and the experimental results. The overall calibration errors of MKM and MLH are similar, but the MKM prediction results of several sets of numerical simulations are very outrageous. Therefore, the prediction effect of the MLH model is better than that of the MKM model to avoid intolerable calibration errors under certain conditions. The prediction results of the ANN model are concentrated on the diagonal line, but the prediction of the yield and fracture position is not as accurate as the hardening interval. In summary, the ANN model is an emerging phenomenological model, which exhibits great advantages in the characterization of electroplastic coupling effects.

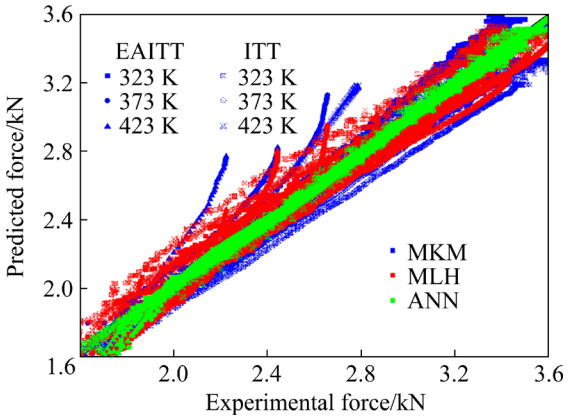

Fig. 17 Comparison of predicted force with experimental one

5 Conclusions

(1) The elongation increases sharply and the flow stress decreases when electric pulse is applied to the deformation process. The 5182-O aluminum alloy exhibits a negative strain rate effect at 323 K, but electrical pulse can promote it to exhibit a positive strain rate effect above 373 K. The effect of electrical pulse on softening and necking strain is relatively large at low strain rates.

(2) The independent contribution of the electrical pulse to the inhibition of serrated flow promotes the stability of the plastic region. The XRD and TEM analysis shows that the dislocation density obtained by EAITT is lower than that obtained by ITT at the same initial temperature.

(3) The limited scope of application of the MKM and the MLH models makes the prediction errors relatively large. The ANN-based hardening model can accurately capture negative strain rate effects, non-monotonic temperature effects and electroplastic effects. The ANN model is able to numerically simulate the plastic response before necking with excellent accuracy compared to the other two analytical models.

(4) The modeling and characterization of electroplastic effects under different coupling effects are of great significance for improving accuracy of forming simulation, reducing manufacturing difficulty and improving surface quality in EAP. The rational application of various effects or mechanisms can break through the manufacturing bottleneck of difficult-to-form materials and promote the development of advanced manufacturing technologies.

CRediT authorship contribution statement

Hong-chun SHANG: Conceptualization, Investigation, Methodology, Writing − Original draft; **Song-chen WANG:** Investigation, Conceptualization, Formal analysis; **Yan-shan LOU:** Conceptualization, Methodology, Investigation, Writing − Review & editing, Supervision.

Declaration of competing interest

The authors declare that they have no known competing financial interests or personal relationships that could have appeared to influence the work reported in this paper.

Acknowledgments

The authors are grateful for the financial supports from the National Natural Science Foundation of China (Nos. 52075423, U2141214).

References

[1] JIAO Zhi-hui, LANG Li-hui, ZHAO Xiang-ni. 5A06-O aluminium–magnesium alloy sheet warm hydroforming and optimization of process parameters [J]. Transactions of Nonferrous Metals Society of China, 2021, 31(10): 2939−2948.

[2] GUAN L, TANG G Y, CHU P K. Recent advances and challenges in electroplastic manufacturing processing of metals [J]. Journal of Materials Research, 2010, 25(7): 1215−1224.

[3] GENG Hui-cheng, WANG Yi-lin, ZHU Bin, WANG Zi-jian, ZHANG Yi-sheng. Effect of solution treatment time on plasticity and ductile fracture of 7075 aluminum alloy sheet in hot stamping process [J]. Transactions of Nonferrous Metals Society of China, 2022, 32(11): 3516−3533.

[4] WU Hui-ping, YANG Wen-bing, PENG He-li, LI Xi-feng, CHEN Jun. Diffusion bonding criterion based on real surface asperities: Modeling and validation [J]. Journal of Manufacturing Processes, 2020, 57: 477−487.

[5] KUANG J, LOW T S E , NIEZGODA S R, LI X H, GENG Y B, LUO A A, TANG G Y. Abnormal texture development in magnesium alloy Mg−3Al−1Zn during large strain electroplastic rolling: Effect of pulsed electric current [J]. International Journal of Plasticity, 2016, 87: 86−99.

[6] LI Xi-feng, WANG Shen, ZHAO Shuang-jun, DING Wei, CHEN Jun, WU Guo-hong. Effect of pulse current on the tensile deformation of SUS304 stainless steel [J]. Journal of Materials Engineering and Performance, 2015, 24(12): 5065−5070.

[7] ROH J H, SEO J J, HONG S T, KIM M J, HAN H N, ROTH J T. The mechanical behavior of 5052-H32 aluminum alloys under a pulsed electric current [J]. International Journal of Plasticity, 2014, 58: 84−99.

[8] LI Da-long, YU En-lin. Computation method of metal's flow stress for electroplastic effect [J]. Materials Science and Engineering A, 2009, 505(1): 62−64.

[9] ZHOU Chang, ZHAN Li-hua, LI He, ZHAO Xing, CHEN Fei, HUANG Ming-hui. Creep ageing behaviour assisted by electropulsing under different stresses for Al−Cu−Li alloy [J]. Transactions of Nonferrous Metals Society of China, 2021, 31(7): 1916−1929.

[10] KIR'YANCHEV N E, TROITSKII O A, KLEVTSUR S A. Electroplastic deformation of metals (review) [J]. Strength of Materials, 1983, 15(5): 709−715.

[11] CONRAD H. Thermally activated plastic flow of metals and ceramics with an electric field or current [J]. Materials Science and Engineering A, 2002, 322(1): 100−107.

[12] CONRAD H. Electroplasticity in metals and ceramics [J]. Materials Science and Engineering A, 287(2): 276−287.

[13] ANDRAWES J S, KRONENBERGER T J, PERKINS T A, ROTH J T, WARLEY R L. Effects of DC current on the mechanical behavior of AlMg1SiCu [J]. Materials and Manufacturing Processes, 2007, 22(1): 91−101.

[14] KIM M J, LEE K, OH K H, CHOI I S, YU H H, HONG S T, HAN H N. Electric current-induced annealing during uniaxial tension of aluminum alloy [J]. Scripta Materialia, 2014, 75: 58−61.

[15] JIANG Yan-bin, TANG Guo-yi, SHEK C H, ZHU Yao-hua, XU Zhuo-hui. On the thermodynamics and kinetics of electropulsing induced dissolution of β-$Mg_{17}Al_{12}$ phase in an aged Mg−9Al−1Zn alloy [J]. Acta Materialia, 2009, 57(16): 4797−4808.

[16] FAN Rong, MAGARGEE J, HU Ping, CAO Jian. Influence of grain size and grain boundaries on the thermal and mechanical behavior of 70/30 brass under electrically-assisted deformation [J]. Materials Science and Engineering A, 2013, 574: 218−225.

[17] JORDAN A, KINSEY B L. Investigation of thermal and mechanical effects during electrically-assisted microbending [J]. Journal of Materials Processing Technology, 2015, 221: 1−12.

[18] KINSEY B, CULLEN G, JORDAN A, MATES S. Investigation of electroplastic effect at high deformation rates for 304SS and Ti−6Al−4V [J]. CIRP Annals, 2013, 62(1): 279−282.

[19] SALANDRO W A, BUNGET C, MEARS L. Modeling and quantification of the electroplastic effect when bending stainless steel sheet metal [C]//ASME International Manufacturing Science and Engineering Conference. Pennsylvania, USA, 2010: 581−590.

[20] REZAEI ASHTIANI H R, SHAYANPOOR A A. New constitutive equation utilizing grain size for modeling of hot deformation behavior of AA1070 aluminum [J]. Transactions of Nonferrous Metals Society of China, 2021, 31(2): 345−357.

[21] CAO Fu-rong, YIN Bin, LIU Si-yuan, SHI Lu, WANG Shun-cheng, WEN Jing-lin. Microstructural evolution, flow stress and constitutive modeling of Al−1.88Mg−0.18Sc−0.084Er alloy during hot compression [J]. Transactions of Nonferrous Metals Society of China, 2021, 31(1): 53−73.

[22] ALI U, MUHAMMAD W, BRAHME A, SKIBA O, INAL K. Application of artificial neural networks in micromechanics for polycrystalline metals [J]. International Journal of Plasticity, 2019, 120: 205−219.

[23] SHANG Hong-chun, ZHANG Chong, WANG Song-chen, LOU Yan-shan. Large strain flow curve characterization considering strain rate and thermal effect for 5182-O aluminum alloy [J]. International Journal of Material Forming, 2023, 16: 1.

[24] LI Xue-yang, ROTH C C, MOHR D. Machine-learning based temperature- and rate-dependent plasticity model: Application to analysis of fracture experiments on DP steel [J]. International Journal of Plasticity, 2019, 118: 320−344.

[25] JORDAN B, GORJI M B, MOHR D. Neural network model describing the temperature- and rate-dependent stress-strain response of polypropylene [J]. International Journal of Plasticity, 2020, 135: 102811.

[26] ZHANG A N, MOHR D. Using neural networks to represent von Mises plasticity with isotropic hardening [J]. International Journal of Plasticity, 2020, 132: 102732.

[27] XU K L, HUANG D Z, DARVE E. Learning constitutive relations using symmetric positive definite neural networks [J]. Journal of Computational Physics, 2021, 428: 110072.

[28] ZHANG Yin, LI Qing-jie, ZHU Ting, LI Ju. Learning constitutive relations of plasticity using neural networks and full-field data [J]. Extreme Mechanics Letters, 2022, 52: 101645.

[29] MOZAFFAR M, BOSTANABAD R, CHEN W, EHMANN K, CAO J, BESSA M A. Deep learning predicts path-dependent plasticity [J]. Proceedings of the National Academy of Sciences, 2019, 116(52): 26414−26420.

[30] GORJI M B, MOZAFFAR M, HEIDENREICH J N, CAO J, MOHR D. On the potential of recurrent neural networks for modeling path dependent plasticity [J]. Journal of the Mechanics and Physics of Solids, 2020, 143: 103972.

[31] SHANG Hong-chun, WANG Song-chen, ZHOU Liu-cheng, LOU Yan-shan. Neural network-based ductile fracture model for 5182-O aluminum alloy considering electroplastic effect in electrically-assisted processing [J]. Engineering Fracture Mechanics, 2023, 290: 109476.

[32] LI X Y, ROTH C C, BONATTI C, MOHR D. Counterexample-trained neural network model of rate and temperature dependent hardening with dynamic strain aging [J]. International Journal of Plasticity, 2022, 151: 103218.

[33] SHANG Hong-chun, WU Peng-fei, LOU Yan-shan, WANG Ji-zhen, CHEN Qiang. Machine learning-based modeling of the coupling effect of strain rate and temperature on strain hardening for 5182-O aluminum alloy [J]. Journal of Materials Processing Technology, 2022, 302: 117501.

[34] JIA Bin, ZHANG Yao-yue, RUSINEK A, XIAO Xin-ke, CHAI Ru-gang, GU Guo-chao. Thermo-viscoplastic behavior and constitutive relations for 304 austenitic stainless steel over a wide range of strain rates covering quasi-static, medium, high and very high regimes [J]. International Journal of Impact Engineering, 2022, 164: 104208.

[35] ZHANG Yong, LIU Jun-peng, CHEN Shu-ying, XIE Xie, LIAW P K, DAHMEN K A, QIAO Jun-wei, WANG Yan-li. Serration and noise behaviors in materials [J]. Progress in Materials Science, 2017, 90: 358−460.

[36] ZHU Xu-hao, LIN Yong-cheng, WU Qiao, JIANG Yu-qiang. Effects of aging on precipitation behavior and mechanical properties of a tensile deformed Al−Cu alloy [J]. Journal of Alloys and Compounds, 2020, 843: 155975.

[37] LIN Y C, DONG W Y, ZHU X H, WU Q, HE Y J. Deformation behavior and precipitation features in a

stretched Al−Cu alloy at intermediate temperatures [J]. Materials, 2020, 13: 2495.
[38] TONG Meng-meng, JIANG Feng, WANG Hui-ling, JIANG Jing-yu, YE Peng-cheng, XU Xu-da. The evolutions of mechanical properties and microstructures of Al−Mg−Mn−Sc−Zr alloy during dynamic stretching deformation [J]. Journal of Alloys and Compounds, 2021, 889: 161753.
[39] WANG Ya-fei, XIA Liu, CAO Yi-tao, ZHANG Hong-jie, HAO Zhong-hu, WU Wei-chao. Imposition of electric current to promote the Portevin-Le Chatelier effect of CoCrFeMnNi high-entropy alloy at low temperatures [J]. Materials Science and Engineering A, 2020, 793: 139893.
[40] XIE Huan-yang, DONG Xiang-huai, LIU Kai, AI Zhen-qiu, PENG Fang, WANG Qian, CHEN Fei, WANG Jian-feng. Experimental investigation on electroplastic effect of DP980 advanced high strength steel [J]. Materials Science and Engineering A, 2015, 637: 23−28.
[41] ALGENDY A Y, LIU K, CHEN X G. Evolution of dispersoids during multistep heat treatments and their effect on rolling performance in an Al−5%Mg−0.8%Mn alloy [J]. Materials Characterization, 2021, 181: 111487.
[42] HAJYAKBARY F, SIETSMA J, BÖTTGER A J, SANTOFIMIA M J. An improved X-ray diffraction analysis method to characterize dislocation density in lath martensitic structures [J]. Materials Science and Engineering A, 2015, 639: 208−218.
[43] LANGFORD J I, WILSON A J C. Scherrer after sixty years: A survey and some new results in the determination of crystallite size [J]. Journal of Alloys and Compounds, 1978, 11(2): 102−113.
[44] WANG Wei, GUO En-yu, CHEN Zong-ning, KANG Hui-jun, CHEN Zhong-jun, ZOU Cun-lei, LI Ren-geng, YIN Guo-mao, WANG Tong-min. Correlation between microstructures and mechanical properties of cryorolled CuNiSi alloys with Cr and Zr alloying [J]. Materials Characterization, 2018, 144: 532−546.
[45] HYDE K B, NORMAN A F, PRANGNELL P B. The effect of cooling rate on the morphology of primary Al3Sc intermetallic particles in Al−Sc alloys [J]. Acta Materialia, 2001, 49(8): 1327−1337.
[46] LI Lin-wei, HAN Zhen-hao, GAO Min-qiang, LI Shao-wei, WANG Hui-hui, KANG Hui-jun, GUO En-yu, CHEN Zong-ning, WANG Tong-min. Microstructures, mechanical properties, and aging behavior of hybrid-sized TiB2 particulate-reinforced 2219 aluminum matrix composites [J]. Materials Science and Engineering A, 2022, 829: 142180.
[47] XU Hui, LIU Xue-bing, ZHANG Di, ZHANG Xin-fang. Minimizing serrated flow in Al−Mg alloys by electroplasticity [J]. Journal of Materials Science & Technology, 2019, 35(6): 1108−1112.
[48] BABU B, LINDGREN L E. Dislocation density based model for plastic deformation and globularization of Ti−6Al−4V [J]. International Journal of Plasticity, 2013, 50: 94−108.
[49] TIWARI J, PRATHEESH P, BEMBALGE O B, KRISHNASWAMY H, AMIRTHALINGAM M, PANIGRAHI S K. Microstructure dependent electroplastic effect in AA 6063 alloy and its nanocomposites [J]. Journal of Materials Research and Technology, 2021, 12: 2185−2204.
[50] KRISHNASWAMY H, KIM M J, HONG S T, KIM D, SONG J H, LEE M G, HAN H N. Electroplastic behaviour in an aluminium alloy and dislocation density based modelling [J]. Materials & Design, 2017, 124: 131−142.
[51] HUH H, AHN K, LIM J H, KIM H W, PARK L J. Evaluation of dynamic hardening models for BCC, FCC, and HCP metals at a wide range of strain rates [J]. Journal of Materials Processing Technology, 2014, 214(7): 1326−1340.
[52] MOLA J, LUAN G Q, HUANG Q L, ULLRICH C, VOLKOVA O, ESTRIN Y. Dynamic strain aging mechanisms in a metastable austenitic stainless steel [J]. Acta Materialia, 2021, 212: 116888.
[53] RUSINEK A, RODRÍGUEZ-MARTÍNEZ J A. Thermo-viscoplastic constitutive relation for aluminium alloys, modeling of negative strain rate sensitivity and viscous drag effects [J]. Materials & Design, 2009, 30(10): 4377−4390.

5182-O 铝合金动态变形过程中电塑性效应的建模与表征

尚宏春，王松臣，娄燕山

西安交通大学 机械工程学院，西安 710049

摘　要：研究并表征电脉冲、温度、应变速率和应变耦合效应对 5182-O 铝合金流动行为和塑性的影响。在相同温度下进行等温拉伸试验和电辅助等温拉伸试验，并将 3 种典型模型嵌入 ABAQUS/Explicit 中进行数值模拟以阐明电塑性效应。结果表明，电脉冲能显著降低合金的变形抗力但提高伸长率。与修正的 Kocks−Mecking 模型相比，所提出的修正 Lim−Huh 模型对高度非线性动态硬化行为的标定精度无明显提高。此外，神经网络模型非常适合描述不同变量耦合作用下的宏观力学响应。

关键词：机器学习；铝合金；电塑性效应；耦合效应；有限元分析

(Edited by Wei-ping CHEN)